Laser-Induced Forward Transfer – Current Approaches and Perspectives for 4D Printing of Batteries

Ulrich Rist*
Institute for Applied Materials
- Applied Materials Physics,
Karlsruhe Institute of Technology
Karlsruhe, Germany
https://orcid.org/0009-0006-3697-1687

Wilhelm Pfleging
Institute for Applied Materials
- Applied Materials Physics,
Karlsruhe Institute of Technology
Karlsruhe, Germany
https://orcid.org/0000-0002-9221-9493

***Abstract* — Direct digital manufacturing is one of the key competencies for accelerating rapid prototyping or the production of individually designed products. Laser-induced forward transfer (LIFT) is a frequently used direct digital manufacturing tool for prototyping and production. In this work, the LIFT process was used to print anodes and cathodes which match each other regarding the areal capacity. For this purpose, the transferred voxel density of the anodes was adjusted to match the areal capacity of the cathodes. Subsequently, the electrodes were assembled as a full-cell in pouch cell design. At the end of the electrochemical priming, the cells reach a charge capacity of up to 151 mAh/g, and more than 400 cycles could be achieved at a C-rate of C/2, including the C-rate analysis, before reaching the end-of-life.**

Keywords — laser-induced forward transfer, direct digital manufacturing, full-cell

I. Introduction

To accelerate technical development rapid prototyping is essential. Here direct digital manufacturing is a key competency [1]. As an additive direct digital manufacturing technology, laser-induced printing is a frequently used tool for the manufacturing of prototypes and also in production. By using CAD software to determine the geometry of the object, laser-induced forward transfer (LIFT) offers the possibility to rapidly implement changes to the prototype or to produce customized architectures. It also offers a highly flexible process for the transfer of a wide range of materials, like liquids and suspensions [2, 3], solid materials [3, 4], and even small components like µLEDs [5] or other small components [6]. Another advantage of the technology is the capability to deposit the materials with high precision. Including all of this, LIFT is an interesting technology with a wide field of applications ranging from research in bio-printing [7] to electronic device production [5]. In batteries, a 3D electrode architecture leads to performance improvements in terms of increased cyclability, power density, and energy density [8]. Here, the LIFT process can help to further accelerate the development of optimized electrode architectures with its high flexibility in making changes to the geometry and printing strategy. In recent works, LIFT was used to print electrodes for lithium-ion batteries. Cathodes were printed [9, 10], which were subsequently structured, electrodes for micro-batteries [11, 12], and anodes for installation in coin-cells [13] including anodes printed with different inks to combine the material advantages [14, 15]. State-of-the-art battery manufacturing techniques such as tape casting or slot die coating have less flexibility in the resulting electrode architecture and the accuracy of active material placement is lower, which is very important in the manufacturing of 3D electrode as shown in [15].

In this work, the focus is on large areal printing compared to our previous work in which electrodes for coin cells were printed [13-15]. In addition, both electrodes, anode and cathode, were printed and then assembled as a full cell in a pouch cell design. For the full cells, care was taken to ensure that the capacity of the printed anodes compared to that of the printed cathodes is set so that an areal capacity ratio of more than one is achieved.

II. Material and Methods

The LIFT process is a laser-induced printing process. A schematic illustration is shown in Fig. 1. The material which is to be transferred is also called “paste”, “slurry” or “ink” in the case of suspensions. It is located on a donor substrate, also called “donor plate” or “ribbon”. By imaging the laser on the interface between the donor plate and the ink, a material transfer is initiated. The transfer is caused by the vaporization of parts of the material [16]. On the opposite side, there is a substrate on which the material is to be printed. As an example, Fig. 2 shows a scanning electron microscope (SEM, PW-100-018, Phenom-World BV, Eindhoven, The Netherlands) image of a LIFT printed voxel with anode ink containing mesocarbon microbeads (MCMB) as active material.

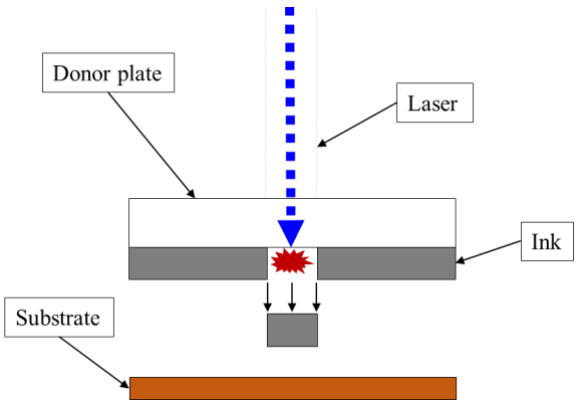

Fig. 1. Schematic illustration of the LIFT process.

A variety of materials can be transferred using the LIFT process. As this is a nozzle-free technology, a wide range of particle sizes and solid contents of suspensions can be printed [17]. For printing, the viscosity of the ink plays an important role in the quality of how well the transferred material reproduces the used laser intensity profile [18].

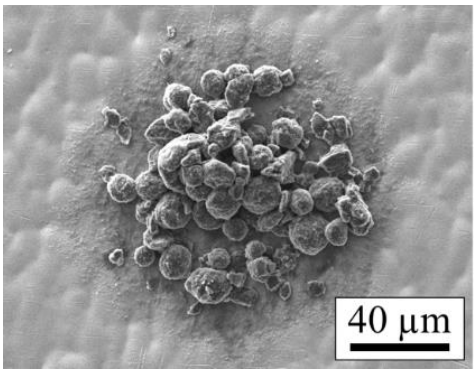

Fig. 2. SEM image of a transferred voxel printed with electrode ink containing MCMB graphite as active material on copper current collector foil.

The used LIFT setup in this work is schematically illustrated in Fig. 3. A frequency tripled Nd:YAG laser source (Lumentum, San Jose, CA, USA, Model: Q301-HD-1000R) with an operational wavelength of 355 nm is applied. The laser radiation has a maximum average power of 10 W, a pulse duration of 78 ns, and a repetition rate of 10 kHz. The Gaussian laser beam is passing through a diffractive optical element that shapes the beam into a 2D top-hat profile. A further shaping of the laser intensity profile is realized by a mask selector. Here, the laser beam can be shaped into squares and circles of different sizes. An objective lens system is finally used to image the mask selector plane with a demagnification factor of 3.5 on the underside of the donor plate which is a quartz glass wafer (DSP-200×0675-SGQ-00, Wafer Universe, Elsoff, Germany). The electrode ink is coated on the donor plate via a doctor blade with a doctor blade gap of 40 µm. On the opposite of the donor plate is the substrate on which the material is printed. In the case of anodes, the substrate is a 9 µm thick copper foil, and in the case of cathodes a 20 µm thick aluminum foil.

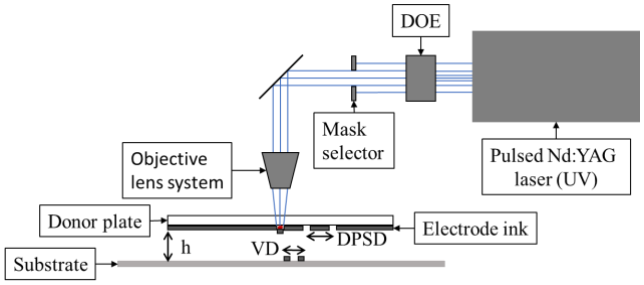

Fig. 3. Schematic illustration of the used LIFT setup.

The schematic illustration (Fig. 3) also displays important printing parameters of the LIFT process. The space (h) between the donor plate and the substrate has an influence on the printing quality [19-21]. Another parameter is the distance between ablations of material on the donor plate (DPSP). It is important that the printing steps are not affected by each other. The last displayed parameter is the voxel distance (VD). A certain overlap of the transferred voxels (Fig. 2) is needed, so that a line or an area can be deposited [22].

The composition of the anode ink used for printing with the LIFT process is displayed in TABLE I. For the full-cell, an optimized composition was taken [23]. For the anodes, graphite (T808, Targray, Kirkland, QC, Canada, d_{50} = 4.9 µm) was used as active material. As the binder, polyacrylic acid (PAA, 306215, Merck, Deutschland) with a molecular weight of 1.25 Mg/mol was taken. To higher the conductivity in the electrode layer carbon black (Super C65, TIMCAL, Bodio, Switzerland) was used.

For the preparation of an anode slurry, PAA was premixed in a solution with a content of 4.13 wt.% with a planetary mixer (SpeedMixer DAC 150 SP, Hauschild, Hamm, Germany) at speeds of up to 3500 rpm for at least 30 minutes until the PAA was dissolved. Then it was stirred for 12 h with a magnetic stirrer. The graphite and carbon black were then added to the PAA solution and mixed with a planetary mixer at speeds of up to 3500 rpm for at least 65 minutes until a homogeneous slurry was obtained.

TABLE I. COMPOSITION OF THE ANODE INKS USED FOR PRINTING THE ANODE FOR ASSEMBLING IN FULL-CELLS AND HALF-CELLS.

Material	**Composition in wt.%**	
	Half-cell	***Full-cell***
Graphite	85	93
PAA	10	5.6
Carbon black	5	1.4

The solid composition of the cathode ink is displayed in TABLE II. Lithium nickel manganese cobalt oxide (NMC622, BASF, Ludwigshafen, Germany) was used as the active material for the cathode electrodes. As the binder polyvinylidene fluoride (PVDF, Solef 5130, Solvay, Brussels, Belgium) was used. To increase the electronic conductivity carbon black (Super C65, Imerys, Paris, France) and conductive graphite (KS6L, Imerys, Paris, France) were added to the slurry.

For the preparation of a cathode slurry, PVDF was premixed with n-methyl-2-pyrrolidone (NMP, Merck, Darmstadt, Germany) with a planetary mixer with a ratio of 1:10 at speeds of up to 3000 rpm for at least 30 minutes until the PVDF is dissolved. The binder solution was left to rest for 12 h. Then NMC622, carbon black, and conductive additive were added to the solution. The slurry was mixed with a planetary mixer with mixing speeds of up to 3500 rpm for at least 70 minutes until a homogenous slurry was obtained.

TABLE II. COMPOSITION OF THE USED CATHODE INK.

Material	**Composition in wt.%**
NMC622	92
PVDF	3
Carbon black	3
Conductive graphite	2

Once the slurry had been prepared, it was printed onto the respective metal foil using the LIFT process. For this purpose, the slurry was coated with a doctor blade with a gap of 40 µm on the donor plate. Subsequently, areas with a rectangular-shaped footprint with a side length of 13 mm were printed on the respective current collector in order to determine the capacitance of the used active materials. Four different axes were used to print the electrodes. The x-axis and the y-axis of the system to determine the position of the transfer on the substrate. In addition, the x-axis and y-axis of the donor plate holder. They were used to ensure that the paste to be transferred was not affected by a previous transfer. After printing and drying of the electrodes, they were cut out with a diameter of 12 mm using a micromachining system (PS450-TO, Optec S.A, Belgium) equipped with an ultrashort pulse (USP) laser (Tangerine, Amplitude Systèmes, France) operating at a wavelength of 515 nm. Subsequently, the electrodes were dried for 24 hours in a vacuum oven at 80 °C for anodes and 130 °C for cathodes. The different

temperatures for the drying process were chosen for PAA due to the glass transition temperature and for PVDF due to the melting point. The difference between the glass transition temperature and the melting point was chosen to be sufficiently large that it can be assumed that the material with the lowest melting point in the electrode - the binder - is not affected by the drying process. They were then transferred to an argon-filled glovebox (LAB master pro sp., M. Braun, Germany) with water and oxygen content < 0.1 ppm. There, the electrodes were assembled in a coin-cell (CR2032) with lithium as counter electrode using 160 µl of electrolyte (Solvionic, France). The electrolyte consists of a mixture of ethylene carbonate (EC) and ethyl methyl carbonate (EMC) with a weight ratio of 3:7 as the solvent, 1.3M lithium hexafluorophosphate ($LiPF_6$) as the conductive salt, and 5 wt.% fluoroethylene carbonate (FEC) as the additive.

For the large format printed batteries, rectangular-shaped footprints with a side length of 29 mm were printed for the cathodes, and rectangular-shaped footprints with a side length of 31 mm for the anodes. Here, each electrode was printed using one donor plate each. After the printing and drying of the electrode layers, they were cut out with the USP laser beam. The anodes were cut with a side length of 30 mm and the cathodes with a side length of 26 mm. Before the printed electrodes were transferred to the argon-filled glovebox, they were dried in a vacuum oven at 60 °C for 24 hours to remove any residual moisture from the electrodes. For the electrochemical analyses in pouch cells, the electrodes were assembled in a state-of-the-art pouch bag. Fig. 4 shows a stacked and not yet sealed pouch cell on the used pouch bag. In the picture, the cathode is at the top, with the separator below and the anode in contact with the pouch bag material.

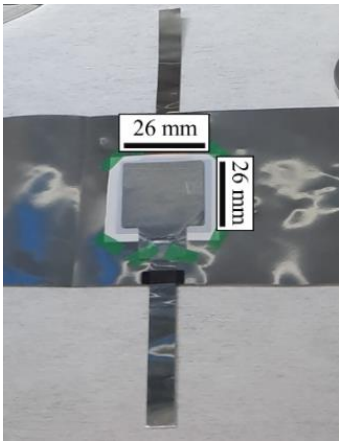

Fig. 4. Image of stacked electrodes of the pouch cell on the pouch bag material.

Subsequently, two of the three open pouch sides were sealed with a vacuum sealing machine (Audionvac VMS 163, Audion Elektro GmbH, Kleve, Germany) and one milliliter of electrolyte was filled in from the third side. Finally, the third side was vacuum sealed. After electrochemical priming, the cell was transferred back into the glovebox. The cell was then opened to allow the, during the priming process, generated gas to dissipate and vacuum sealed again.

After cell assembly, the cells were electrochemically characterized with a BT 2000 (Arbin Instruments, College Station, TX, USA). After 20 h of waiting, the cells were charged with a constant current (CC) to 4.2 V, and then they were charged at a constant voltage (CV) to a cut-off current, displayed in TABLE III and TABLE IV. For the discharging process, the cell is discharged with a constant current to 3 V. For the electrochemical characterization the cells were first primed with the protocol displayed in TABLE III.

TABLE III. PRIMING PROCEDURE FOR FULL-CELLS, INCLUDING THE C-RATE FOR CHARGING AND DISCHARGING, THE CUT-OFF C-RATE AT THE CV-PHASE, AND THE NUMBER OF CYCLES AT EVERY C-RATE.

Charge current	C/50	C/20
Cut-off	C/100	C/50
Discharge current	C/50	C/20
Cycle number	1	3

Subsequently to the priming procedure, the cells were characterized by a C-rate analysis. For this purpose, the cells were charged with different C-rates from C/10 to 5C, as displayed in TABLE IV. The second C/5 cycles at the end of the analysis were used as a control measurement to compare the charge capacity achieved in the C/5 cycles at the beginning of the analysis with the C/5 cycles at the end of the analysis so that a capacity loss can be determined.

TABLE IV. C-RATE ANALYSIS FOR FULL-CELLS, INCLUDING THE C-RATE FOR CHARGING AND DISCHARGING, THE CUT-OFF C-RATE AT THE CV-PHASE, AND THE NUMBER OF CYCLES AT EVERY C-RATE.

Charge current	C/10	C/5	C/2	1C	2C	3C	5C	C/5
Cut-off	C/20	C/10	C/10	C/10	C/10	C/10	C/10	C/10
Discharge current	C/10	C/5	C/5	C/5	C/5	C/5	C/5	C/5
Cycle number	5	5	5	5	5	5	5	5

With an anode half-cell, the charging and discharging protocol (CCCV-phase and CC-phase) is reversed and the voltage window is between 0.01 V and 1.5 V. For the cathode half-cells, the voltage window in which the batteries were cycled was from 3 V to 4.3 V. Apart from the exceptions mentioned for each half-cell, electrochemical priming and C-rate analysis were performed as shown in TABLE III and TABLE IV.

III. RESULTS AND DISCUSSION

To calculate the capacity of the electrodes of the full-cells, the specific capacity of the active materials had to be determined for each active material. For this purpose, electrodes were printed for each cathode and anode and characterized against lithium in a half-cell. The characterization of the anode material is displayed in Fig. 5

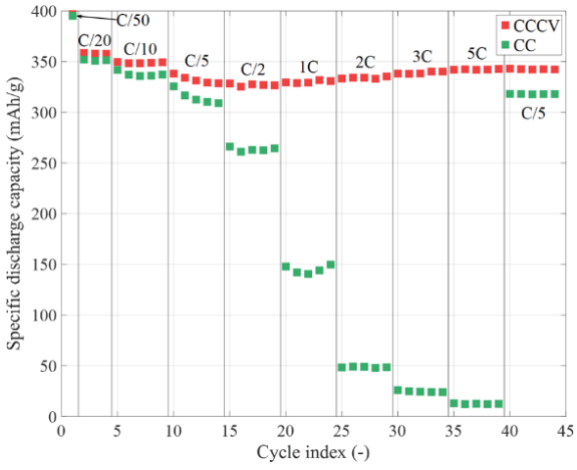

Fig. 5. Specific discharge capacity of the C-rate analysis of the printed anode half-cell. The capacity of the CCCV-phase is shown in red and that with the CC-phase in green (Capacity retention: 102 %).

For the graphite half-cells, the specific discharge capacity is displayed as a function of the cycle index. The chemical process in the anode during discharge in a half-cell is the intercalation of lithium into the graphite, which is the same process occurring during charging of the anode in a full-cell. The active material obtains a specific discharge capacity at the last C/20 cycle of the electrochemical priming of 358 mAh/g. The capacity that can be discharged during the CC-Phase decreases with increasing C-rate. The capacity retention after the analysis is 102 % and displays that the material is not degraded even after high currents of 5C. It seems that after the first C/5 cycles some active material was reactivated during the characterization.

The characterization of the used active material for the cathodes is displayed in Fig. 6.

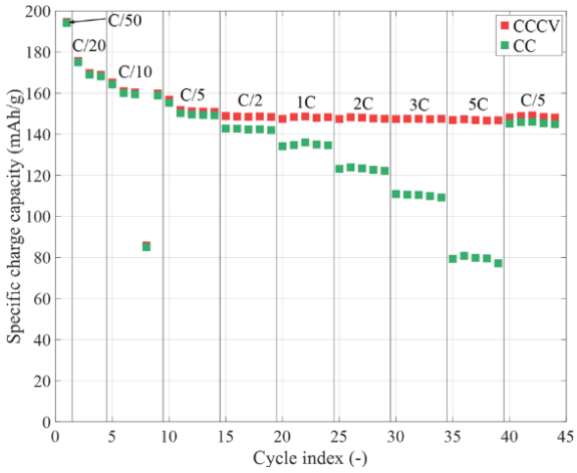

Fig. 6. Specific charge capacity of the C-rate analysis of the printed cathode half-cell. The capacity of the CCCV-phase is shown in red and that with the CC-phase in green (Capacity retention: 98 %). The one lower capacity at C/10 seems to be a technical problem, as the specific capacity continues to run as expected afterwards.

The specific charge capacity for the cathode half-cell is displayed over the cycle index. The electrode exhibits a specific charge capacity of 169 mAh/g at the last cycle of the electrochemical priming. At 5C, still almost half of the capacity is charged during the CC-phase, which shows a high performance at higher currents. The capacity retention at the end of the C-rate analysis is 98 %, which indicates that there is only a small amount of active material degraded during the analysis.

As described above, for full-cells the areal capacity of the anodes has to be higher than the one of the cathodes, so that the balancing between these electrodes is greater than one. For this purpose, the cathodes and anodes were printed first. Then the capacities of the electrodes were determined by weighing the electrodes. The capacities were calculated with the mass of the electrode, the composition of the electrode, the density of the specific materials, and the before-measured specific capacity of the active material. As displayed in TABLE V, the average areal capacity of the cathodes is 0.76 mAh/cm^2. As applying the first printing parameters of the anodes (Anode 1) only an average areal capacity of 0.53 mAh/cm^2 was obtained. In previous works, the capacity was adjusted by multilayer printing [13]. Since this method only allows the areal capacity to be adjusted by multiplicative integers, it was adjusted in this work by adjusting the printed voxel density. The printed voxels per square millimeter were adjusted (TABLE V) and the customized printed anode (Anode 2) has an average areal capacity of 0.89 mAh/cm^2, which is higher than the one of the cathodes and therefore matches it. It can therefore be stated that the capacity can also be adjusted by setting the printed voxels per square millimeter to print electrodes with a customized areal capacity. In addition to the realized area output and the voxel density, the applied printing speed and the resulting time for the large-scale electrodes are also shown in TABLE V. The applied printing speed was set due to the limitations of the axis speed of the applied setup. It can be seen, that the Anode 2 electrodes needed more time to print due to the higher voxel density.

To further speed up the process the printing strategy needs to be changed, for example by using a scanner to guide the laser beam. A possible printing strategy with the scanner would be, for example, to print only every second voxel and then bring the donor plate into a position in which no transfer has yet taken place and then print the missing voxels, so the transfer is not affected by a previous transfer. Such printing strategies can speed up the process enormously. In addition, multi-beam printing using beam splitters and a continuous supply of fresh donor plate material, e.g. by roll-to-roll, would be needed to achieve the processing speeds required for industrial-scale production. Henning et. al. [24] presented a setup for a LIFT system with continuous material feed and increased throughput. However, the main benefit of this technology is the ability to create customized electrodes by precisely positioning of material for micro-batteries or prototyping.

TABLE V. AVERAGE REALIZED AREAL CAPACITY FOR THE VOXELS PER MM^2 OF THE PRINTED CATHODES, OF THE FIRST PRINTED ANODES (ANODE 1), AND THE CUSTOMIZED PRINTED ANODES (ANODE 2), REGARDING THE AREAL CAPACITY OF THE CATHODES. ADDITIONALLY, THE POSSIBLE PRINTING SPEED (LIMITED BY THE PRINTING STRATEGY AND THE SETUP LIMITS) AND THE RESULTING PROCESSING TIME.

Electrode	Realized areal capacity in mAh/cm^2	Voxels per mm^2 in -	Printing speed in mm/s	Time in min
Cathode	0.76	69.44	4	37
Anode 1	0.53	69.44	4.5	38
Anode 2	0.89	131.81	3.5	65

For the printing of the large-size electrodes different laser parameters were applied for printing the anode and the cathode material. As comparing the laser parameters displayed in TABLE VI, it can be seen, that the cathode material needed less laser power to transfer a voxel.

TABLE VI. LASER PARAMETER FOR THE PRINTING OF THE ELECTRODES

Electrode	Power in W	Fluence in J/cm^2	Peak energy in µj
Cathode	1.20	0.36	111
Anode	1.89	0.57	175

The electrodes with the customized parameters were printed, the capacitance was calculated from the mass of the electrodes, and they were then matched, see TABLE VII. The balancing of the anodes and cathodes is higher than one, which had to be fulfilled as a matching criterion.

TABLE VII. CAPACITY OF THE ANODE AND CATHODES AND THE BALANCING OF THE ASSEMBLED FULL-CELLS.

Cell	Areal capacity in mAh/cm^2		Balancing in -
	Cathode	*Anode*	*N/P*
1	0.76	0.87	1.15
2	0.76	0.90	1.19

After the assembling of the full-cells, the cells were electrochemically primed and a C-rate analysis took place. The results of the C-rate analysis of the full-cell are shown in Fig. 7.

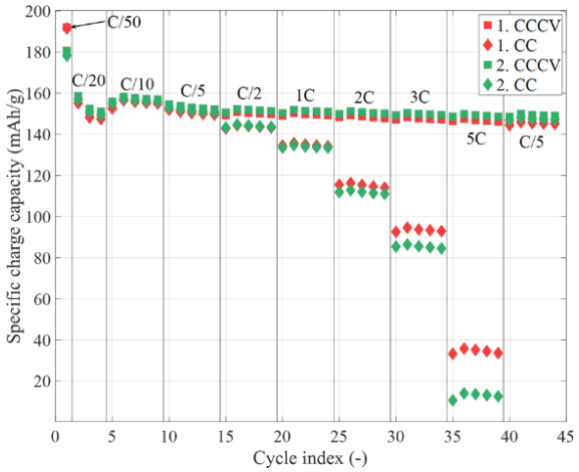

Fig. 7. Specific charge capacity of the C-rate analysis of the full-cells. The capacity of cell 1 is shown in red and that of cell 2 in green (Capacity retention: 97 % and 98 %, respectively). The capacity of the CCCV-phase is shown in squares and that of the CC-phase in diamonds.

In the diagram, the specific charge capacity is displayed as a function of the cycle index. Cell 1 and cell 2 obtain a specific charge capacity of 149 mAh/g and 151 mAh/g, respectively. At the C/10 cycle, there is a small increase in the capacity observable. This could be due to improved contacting of the electrodes through degassing and subsequent resealing under vacuum after electrochemical priming. Following C-rate analysis, only minor electrochemical degradation is detected, with capacity retention of 97% (cell 1) and 98% (cell 2). However, as the degradation is quite low, it can be stated that both printed electrodes have a quite common, usual electrochemical behavior.

As the electrodes only degraded slightly during the C-rate analysis, a long-term test was subsequently initialized. The cycling sequence was 50 times C/2 cycles followed by 5 times C/5 check-up cycles to determine the degradation of the cells. The results of the long-term analysis are displayed in Fig. 8.

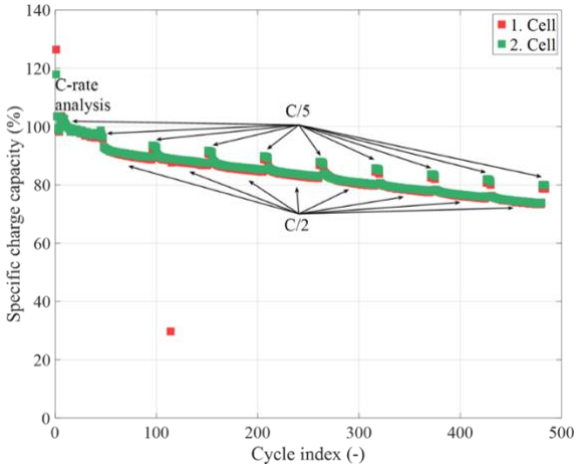

Fig. 8. Percentage charge capacity of the long-term test of the full cells of the CCCV-phase to the average capacity of the first 5 C/5 cycles (C-rate analysis). The capacity of cell 1 is shown in red and that of cell 2 in green (Capacity retention at 484 cycles: 78 % and 79 %, respectively). The cycle sequence was 50 cycles at C/2 followed by 5 cycles at C/5. The one lower capacity of Cell 1 at the second 50 C/2 cycles appears to be a technical issue, as the specific capacity afterwards continues as expected.

Here, the percentual charge capacity in comparison to the average capacity of the first 5 C/5 cycles is shown as a function of the cycle index. In the diagram, only the CCCV-phase is displayed. The first 44 cycles display the C-rate analysis shown in Fig. 7. With increasing cycling numbers an increasing degradation of the batteries can be observed. In the control cycles, the batteries reached slightly less than 80% of the average capacity of the first 5 C/5 cycles after more than 480 cycles and thus the end-of-life was reached. The electrochemical data from the long-term analysis also show, as the C-rate analysis, a quite uniform electrochemical behavior.

IV. Conclusion and Outlook

The printing of cathodes and anodes was realized via the LIFT process. To print electrodes for a full-cell first the specific capacity of the active materials of the printed anode and printed cathode was determined. The specific capacity of the active materials was analyzed to ensure that the areal capacity of the electrodes matched and that the one of the anodes was higher than that of the cathodes. For this purpose, half-cells were assembled and characterized with a printed anode and a printed cathode against lithium. Then the capacity of the large field printings was calculated including the mass of the electrode, the composition of the electrode, the density of the specific materials, and the before-measured specific capacity of the active material. With this information, it was possible to adjust the areal capacity of the anode, regarding the one of the cathode, by adjusting the printed voxel density, in contrast to previous work where the capacity was adjusted by the printing of multilayer [13]. With the customized anodes, full-cells with an anode size of 30x30 mm^2 and a cathode size of 26x26 mm^2 were assembled as a pouch cell design. The cells reached a specific capacity of up to 151 mAh/g at the last cycle of the electrochemical priming. In addition, the cells showed a high capacity retention of up to 98 % after the C-rate analysis. In the subsequent long-term test, they were able to run through more than 400 cycles at C/2 before the capacity in the C/5 control cycles was only 80 % of the original capacity. This makes it possible to print individually designed electrodes with a customized areal capacity using the LIFT process.

In the following, the correlation between printed voxel density and areal capacity must be investigated further. In addition, the electrodes must be further developed in the direction of the state-of-the-art volume density including the calendering process and areal capacity. In addition, the cathode ink can be further developed concerning a non-toxic, printable binder-solvent system, which is already under development for conventional cathode coatings [25, 26].

Acknowledgment

The authors would like to thank M. Kapitz for his continuous support and assistance in the adjustment and development of the laser processing system. We would also like to thank A. Reif for her help in operating the SEM.

This project has received funding from the German Research Foundation (DFG, project No. 467624762) and scientific research exchange supported by EU-L4DNANO (HORIZON, project No. 101086227)

References

[1] J. Holmström, M. Holweg, S. H. Khajavi, and J. Partanen, "The direct digital manufacturing (r)evolution: definition of a research agenda," *Operations Management Research*, vol. 9, no. 1-2, pp. 1-10, 2016, doi: 10.1007/s12063-016-0106-z.

[2] J. M. Fernández-Pradas, "Laser-Induced Forward Transfer of Fluids," in *Laser Printing of Functional Materials. Electronics, 3D Microfabrication and Biomedicine*, A. Pique´ and P. Serra Eds., 1. Auflage ed. Newark: John Wiley & Sons Incorporated, 2018, pp. 63-89.

[3] P. Sopeña, J. M. Fernández-Pradas, and P. Serra, "Laser-induced forward transfer of low viscosity inks," *Applied Surface Science*, vol. 418, pp. 530-535, 2017, doi: 10.1016/j.apsusc.2016.11.179.

[4] A. Piqué, R. C. Y. Auyeung, H. Kim, N. A. Charipar, and S. A. Mathews, "Laser 3D micro-manufacturing," *Journal of Physics D: Applied Physics*, vol. 49, no. 22, p. 223001, 2016, doi: 10.1088/0022-3727/49/22/223001.

[5] O. Haupt, J. Brune, M. Fatahilah, and R. Delmdahl, "MicroLED´s: high precision large scale UV laser lift-off and mass transfer processes," presented at the Laser-based Micro- and Nanoprocessing XVI, 2022.

[6] C. B. Arnold *et al.*, "Assembly and integration of thin bare die using laser direct-write," presented at the Photon Processing in Microelectronics and Photonics VI, 2007.

[7] P. Karakaidos, C. Kryou, N. Simigdala, A. Klinakis, and I. Zergioti, "Laser Bioprinting of Cells Using UV and Visible Wavelengths: A Comparative DNA Damage Study," *Bioengineering (Basel)*, vol. 9, no. 8, Aug 9 2022, doi: 10.3390/bioengineering9080378.

[8] W. Pfleging, "Recent progress in laser texturing of battery materials: a review of tuning electrochemical performances, related material development, and prospects for large-scale manufacturing," *International Journal of Extreme Manufacturing*, vol. 3, no. 1, pp. 012002-012022, 2021, doi: 10.1088/2631-7990/abca84 S1 - 21 M4 - Citavi.

[9] J. Pröll, H. Kim, A. Piqué, H. J. Seifert, and W. Pfleging, "Laser-printing and femtosecond-laser structuring of LiMn2O4 composite cathodes for Li-ion microbatteries," *Journal of Power Sources*, vol. 255, pp. 116-124, 2014, doi: 10.1016/j.jpowsour.2013.12.132.

[10] P. Smyrek, H. Kim, Y. Zheng, H. J. Seifert, A. Piqué, and W. Pfleging, "Laser printing and femtosecond laser structuring of electrode materials for the manufacturing of 3D lithium-ion micro-batteries", Proc. of *SPIE*, vol. 9738, (2016), in SPIE Proceedings, pp. 9738061-9738065, doi: 10.1117/12.2211546.

[11] H. Kim, R. C. Y. Auyeung, and A. Piqué, "Laser-printed thick-film electrodes for solid-state rechargeable Li-ion microbatteries," (in English), *Journal of Power Sources*, vol. 165, no. 1, pp. 413-419, Feb 25 2007, doi: 10.1016/j.jpowsour.2006.11.053.

[12] H. Kim, T. E. Sutto, J. Proell, R. Kohler, W. Pfleging, and A. Piqué, "Laser-printed/structured thick-film electrodes for Li-ion microbatteries", Proc. of *SPIE*, vol. 8968, (2014), in SPIE Proceedings, pp. 89680L1-89680L9, doi: 10.1117/12.2037287.

[13] U. Rist, A. Reif, and W. Pfleging, "Laser-induced forward transfer as a versatile tool for developing silicon-based anode materials", Proc. of *SPIE*, vol. 11989, (2022), pp. 119890C1-119890C10, doi: 10.1117/12.2609588.

[14] U. Rist, V. Falkowski, and W. Pfleging, "Electrochemical Properties of Laser-Printed Multilayer Anodes for Lithium-Ion Batteries," (in eng), *Nanomaterials (Basel)*, vol. 13, no. 17, pp. 1-20, Aug 25 2023, doi: 10.3390/nano13172411.

[15] U. Rist, Y. Sterzl, and W. Pfleging, "Laser-induced forward transfer (LIFT) process for flexible construction of advanced 3D silicon anode designs in high-energy lithium-ion batteries", Proc. of *SPIE*, vol. 12873, (2024), pp. 128730F1-128730F8, doi: 10.1117/12.3003087.

[16] P. Serra and A. Piqué, "Laser-Induced Forward Transfer: Fundamentals and Applications," (in English), *Advanced Materials Technologies*, vol. 4, no. 1, pp. 1800099-1800132, Jan 2019, doi: 10.1002/admt.201800099.

[17] P. Serra and A. Piqué, "Introduction to Laser-Induced Transfer and Other Associated Processes," in *Laser Printing of Functional Materials. Electronics, 3D Microfabrication and Biomedicine*, A. Pique´ and P. Serra Eds., 1. Auflage ed. Newark: John Wiley & Sons Incorporated, 2018, pp. 3-13.

[18] S. A. Mathews, R. C. Y. Auyeung, H. Kim, N. A. Charipar, and A. Piqué, "High-speed video study of laser-induced forward transfer of silver nano-suspensions," (in English), *Journal of Applied Physics*, vol. 114, no. 6, p. 064910, Aug 14 2013, doi: 10.1063/1.4817494.

[19] M. Duocastella, M. Colina, J. M. Fernández-Pradas, P. Serra, and J. L. Morenza, "Study of the laser-induced forward transfer of liquids for laser bioprinting," (in English), *Applied Surface Science*, vol. 253, no. 19, pp. 7855-7859, Jul 31 2007, doi: 10.1016/j.apsusc.2007.02.097.

[20] M. Makrygianni, I. Kalpyris, C. Boutopoulos, and I. Zergioti, "Laser induced forward transfer of Ag nanoparticles ink deposition and characterization," (in English), *Applied Surface Science*, vol. 297, pp. 40-44, Apr 1 2014, doi: 10.1016/j.apsusc.2014.01.069.

[21] L. Rapp, J. Ailuno, A. P. Alloncle, and P. Delaporte, "Pulsed-laser printing of silver nanoparticles ink: control of morphological properties," (in eng), *Opt Express*, vol. 19, no. 22, pp. 21563-74, Oct 24 2011, doi: 10.1364/OE.19.021563.

[22] A. Palla-Papavlu, C. Córdoba, A. Patrascioiu, J. M. Fernández-Pradas, J. L. Morenza, and P. Serra, "Deposition and characterization of lines printed through laser-induced forward transfer," (in English), *Appl Phys a-Mater*, vol. 110, no. 4, pp. 751-755, Mar 2013, doi: 10.1007/s00339-012-7279-6.

[23] J. Kumberg *et al.*, "Drying of Lithium‐Ion Battery Anodes for Use in High‐Energy Cells: Influence of Electrode Thickness on Drying Time, Adhesion, and Crack Formation," *Energy Technology*, vol. 7, no. 11, p. 1900722, 2019, doi: 10.1002/ente.201900722.

[24] G. Hennig, G. Hochstein, and T. Baldermann, "Industrial, Large-Area, and High-Throughput LIFT/LIBT Digital Printing," in *Laser Printing of Functional Materials. Electronics, 3D Microfabrication and Biomedicine*, A. Pique´ and P. Serra Eds., 1. Auflage ed. Newark: John Wiley & Sons Incorporated, 2018, pp. 375-403.

[25] B. Boz *et al.*, "Evaluating Polyacrylic Acid as a Universal Aqueous Binder for Ni‐rich Cathodes NMC811 and Si Anodes in Full cell Lithium‐ion Batteries," *ChemPlusChem*, 2024, doi: 10.1002/cplu.202400195.

[26] P. Zhu, V. Trouillet, S. Heißler, and W. Pfleging, "Laser structuring of high mass loaded and aqueous acid processed Li(Ni0.6Mn0.2Co0.2)O2 cathodes for lithium-ion batteries," *Journal of Energy Storage*, vol. 66, 2023, doi: 10.1016/j.est.2023.107401.